Rydberg atom spectroscopy enabled by blackbody radiation ionization

Xiaoxu Lu, Yuan Sun, and Harold Metcalf
Physics and Astronomy, Stony Brook University, Stony Brook, New York 11794-3800, USA
(Received 13 June 2011; published 6 September 2011)

We have excited helium atoms from their metastable $2\,^3S$ state to Rydberg states in the range $13 < n < 50$ in a two-step process via the $3\,^3P$ state using light at $\lambda = 389$ nm and 785–815 nm. Atoms in a thermal beam (100 K) cross partially overlapping laser beams of the appropriate frequencies in the counterintuitive order to exploit the high efficiency of stimulated rapid adiabatic passage. The interaction region is between two plates that can be used for Stark tuning in a few V/cm field or for field ionization. At fields much too low for field ionization, we observe signals attributed to ionization by blackbody radiation. Multiple tests confirm this attribution as the cause of ionization. For example, by heating the plates we observe the expected signal increases. Our experiments reinforce previous work where the interaction between Rydberg atoms and room temperature blackbody radiation is important for experiments.

DOI: 10.1103/PhysRevA.84.033402 PACS number(s): 32.80.Ee

I. INTRODUCTION

Rydberg atoms have attracted widespread attention as tools for many applications in atomic physics, quantum information science, plasma physics, and as an object of study themselves. Their properties have been thoroughly discussed in hundreds of articles, and an important presentation of early work with references is in Ref. [1]. Our research on Rydberg atoms stems from using inhomogeneous electrostatic fields to control their motion for use in atom optics, not only for its intrinsic importance to atomic physics but also for applications such as lithography and atom interferometry.

The usual production and detection methods of Rydberg atoms have been known since the advent of tunable lasers in the early 1970s. Briefly, one or more laser beams can be tuned to the desired atomic transition (or stepwise excitation scheme) and applied either cw or pulsed to a sample of atoms. Detection is almost always by ionization, either with additional radiation or by a modest dc electric field. Radiative ionization works even at very low frequencies because these highly excited states are quite weakly bound. The binding energy for $n = 25$ is only ∼20 meV, whereas blackbody radiation (BBR) peaks at ∼125 meV for $T \sim 300$ K. Field ionization is quite effective for a similar reason, and most states can be ionized by a few hundred V/cm. State selectivity naturally accompanies the field ionization detection method because its threshold is $\mathcal{E}_{FI} = (5 \times 10^9/16n^4)$ V/cm.

Radiative transitions between two Rydberg states and to the continuum, induced by ambient BBR, were studied in the early days of Rydberg atom spectroscopy [2–7] and continue to be a topic of great current interest [8–10]. Although typical BBR ionization rates are in the kHz range, they are still sufficient to ionize a small fraction of the Rydberg atoms in a thermal beam.

There are several new topics presented in this work. The first is the substantially increased sensitivity to the very small fraction of thermal Rydberg atoms ionized by BBR, demonstrating that no additional ionization procedure is needed for observation and accurate measurement. Simply by tuning a weak dc electric field (few V/cm) or the laser frequency, we can resolve fine details of the Stark spectrum. The second is the application of the high efficiency of stimulated rapid adiabatic passage excitation (STIRAP) for the spectroscopy of these states over a wide range of n [11–13]. This has been demonstrated before [14–16] but not with both the resolution and efficiency that we can achieve. The third is an approximate corroboration of the calculations of Ref. [10] and our rate equation description of the redistribution of atoms among Rydberg states. The "reservoir" idea proposed here has been used before [17] but is of importance to quantum information studies as well as the properties of cold neutral plasmas. Finally, we are developing a method for absolute measurement of the efficiency of STIRAP that is used here [18] and will be reported in a later paper [19].

II. EXPERIMENT

In the present experiments we use helium excited to Rydberg states in two steps from the $2\,^3S$ metastable state (He*) [20–22] with state selectivity implemented spectroscopically on the upper transition. We detect excitation to the Rydberg states by measuring the ions produced by BBR at the ambient temperature (∼300 K). The ionization process is a mixture of single-step photoionization and diffusion among Rydberg states but always driven by the local thermal radiation field, as will be discussed below.

A. Helium source and atomic beam detection

The details of the atomic beam properties and geometry will be important later and so are presented here. The He* atoms are produced in a reverse flow dc discharge source labeled A in Fig. 1 [23,24]. It has a slightly supersonic longitudinal velocity distribution of halfwidth ∼± 230 m/s centered near 1070 m/s. This horizontal atomic beam (dashed line in Fig. 1) is collimated to ±2 mrad by a rectangular aperture 0.3 mm wide by 0.5 mm high that subtends $\sim 2.5 \times 10^{-6}$ sr located ∼23 cm away from the 0.5-mm-diam source aperture (B in Fig. 1).

The source output is about 10^{14} He* atoms/sr s, a few parts in 10^6 of the total He flux. The He* flux of $\sim 2.5 \times 10^8$/s through the collimating aperture expands to ∼ 1.2 mm × 1.5 mm at the beam's transverse extrema in the interaction region ∼25 cm downstream from the aperture (C in Fig. 1).

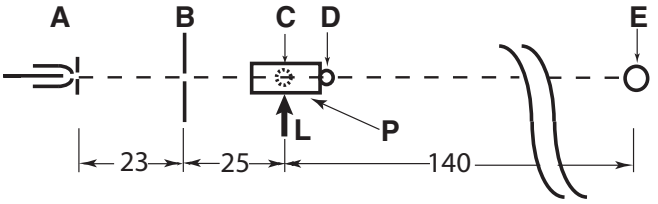

FIG. 1. A top view of the atomic beam setup shows the position of the plates, aperture, and detectors (all dimensions in cm). The dashed line is the beam, A indicates the source region, B is the collimating aperture, and E is the beam detector. The laser beams (L) cross the atomic beam at right angles and the crossing point can be moved along the beam direction by the extent of the the Stark tuning plates P. The detector was first at D but was later moved to C (see text).

Most of the He* atoms are concentrated in the central region of the beam where the average density is $\sim 1.4 \times 10^5/\text{cm}^3$. The flux and density of ground-state He atoms are $\sim 5 \times 10^5$ times larger. The collisional mean free path for He* on He* that can cause Penning ionization at this density is $\sim 5 \times 10^7$ m using the approximate geometric cross section 10^{-15} cm^2. Collisions of He* on ground-state He or background gas also have negligible effect on the populations.

The source produces both He* and uv light and these are distinguished by time-of-flight measurement when we use a chopper in the atomic beam line. They can also be separated by deflection of the atoms with an auxiliary laser beam. The flux of the uv light is approximately the same as that of the He*. Their ratio depends strongly on the discharge parameters (pressure, current, and voltage), and it was found that higher pressure increases the amount of uv light and inhibits production of He*.

The He* atoms fly 1.4 m through the vacuum system to a a beam detector where they strike a multichannel plate (MCP) and easily eject electrons from its upstream side because they carry ~20 eV of internal energy (E in Fig. 1). The output electron bunches of this beam detector can be accelerated to a phosphor screen that is viewed by a charge-coupled device (CCD) camera whose image is stored in a PC.

Because of the nonlinearities of the phosphor/CCD detector, we also use another configuration of this beam detector. In this scheme He* atoms strike a stainless steel target plate where liberated electrons are accelerated to the MCP, and the total output charge is collected on an anode. The anode current is measured by a pico-ammeter and typical values are ~6 nA after $\sim 3 \times 10^4$ amplification by the MCPs. Since the electron ejection efficiency is ~70%, this corresponds to a count rate of $\sim 2 \times 10^6$/s, and this value is corroborated when we use the anode in pulse-counting mode into 50 Ω.

There are several independent causes that each contribute some signal reduction from the estimated $\sim 10^8$ He*/s emerging from the rectangular collimation aperture. These include, but are not limited to, the effect of the 2-mm vertical slit aperture in front of the target plate of the detector (placed for approximate beam spread profiling), the residual beam spread from the collimation (few mrads), the additional spreading from the laser deflection (a few more mrads), the estimated 75% efficiency of the deflection process, and the 70% efficiency of electron ejection by a He* atom.

B. Laser system and excitation region

We excite He* atoms in our beam to principal quantum numbers n ranging from the low teens to the mid 50s. The excitation process requires light at $\lambda = 389$ nm for the $2\,^3S \rightarrow 3\,^3P$ transition and in the 785- to 815-nm region for the $3\,^3P \rightarrow n\,^3S, n\,^3D$ transitions, as shown in Fig. 2.

To induce the uv step of excitation, a commercial frequency doubled Nd:YVO4 laser (Coherent Verdi V10) is used to pump a Ti:Sapphire laser (TiS). The output from the TiS is frequency doubled by a lithium niobate crystal (LBO) in a commercial external build-up cavity (Coherent MBD-200) to produce light at $\lambda = 389$ nm. This doubling cavity is locked to the TiS laser frequency and a small part of the uv light is used in a saturation spectroscopy scheme to lock the TiS to 1/2 of the atomic resonance frequency [25]. The uv light is transmitted to the atomic beam apparatus by an appropriate single-mode fiber for alignment convenience and to assure a good spatial intensity distribution. The ir light in the $\lambda = 785$–815 nm wavelength region is produced by a second TiS pumped by another Verdi V10 laser. It is locked to its own internal, unstabilized etalon.

Both laser beams are focused by cylindrical optics to ellipses whose full-width-at-half-maximum (FWHM) intensity points are 2 mm vertically and 0.5 mm horizontally and cross the atomic beam at a right angle (L in Fig. 1). Even though the vertical atomic beam waist size is large (1.7 mm FWHM), atoms at its vertical extrema experience a Rabi frequency that is more than 80% of the maximum at the laser beam center. The power of the uv beam is ~10 mW and of the ir beam is ~1 W so the Rabi frequencies for each transition ($n \sim$ mid 20s) is ~15 MHz, corresponding to ~8 Rabi oscillations during the 0.5-μs passage time through each laser beam.

The excitation region is between two highly polished and parallel aluminum field plates, about 7×17 cm and separated by ~6 mm (P in Fig. 1 and shown in Fig. 3). A voltage difference can be applied to produces a small dc electric field that enables Stark tuning of the excitation process.

C. Ion detector

As described above, there are two detector systems. The beam detector is about 1.4 m downstream of the interaction

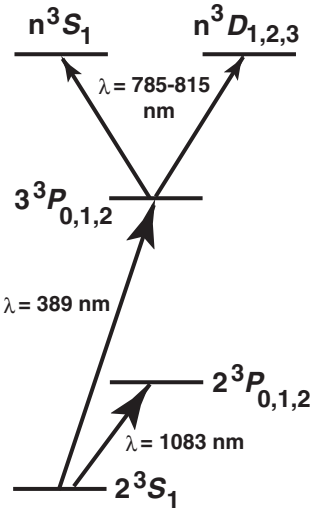

FIG. 2. The excitation level scheme used in our experiments.

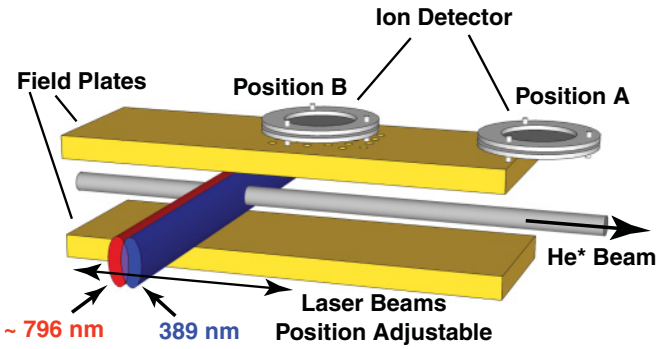

FIG. 3. (Color online) This diagram of the interaction region shows the atomic beam passing between the field plates from left to right, the overlapped laser beams crossing it at angle $\pi/2$, and the ion detector. In earlier experiments the upper plate was solid and the detector was mounted at position A just downstream of the end of the plates. In later experiments the upper plate was replaced by one with an array of 30 holes 0.5 mm diam spaced by ∼4 mm arranged in a triangular array near its center (also shown), and the detector mounted at position B just above these holes. The laser beams can be moved relative to one another and along the He* beam by almost the full length of the plates.

region and is used for observing the He* atoms as discussed in Sec. II A. The ion detector is part of the interaction region and is located just beyond the field plates, above the atomic beam, as shown at D in Fig. 1 and A in Fig. 3. The electron shower of this ion detector is initiated by ions accelerated toward its MCP surface by a −1600 V potential, sufficient to direct them to the MCP and cause electron ejection. It measures the ionized Rydberg atoms by amplifying their current using a second MCP whose output pulse is attracted to a metal anode. As with the downstream beam detector, the ion detector can operate in current mode or in pulse-counting mode.

From such measurements we can extract the MCP gain, the ionization rates, and many other useful parameters. In particular, the 5-ns voltage pulses with 50 Ω across the anode have amplitude of 3 mV that means the MCP gain is $\sim 2 \times 10^6$ at the voltages we use (corresponding to device specifications for these higher voltages compared to those of the beam detector). The 40-nA dc current that we measure by exciting the 24 S state, therefore, corresponds to a count rate of 1.2×10^5, and in pulse-counting mode we measure $\sim 10^5$/s. These similar numbers are about 1000 times less than the estimated 10^8 Rydberg atom flux and will be discussed below.

III. RESULTS

A. Rydberg-Stark spectroscopy

We have examined the spectrum of several different n states of He in a weak electric field. Typically we fix the frequency of the $\lambda \approx 785$–815 nm ir laser and scan the voltage across the plates, although we can also fix the voltage and scan the laser frequency as in Sec. III D. We have not made careful Stark maps of the energy level structure from all these n states, but we find that we can easily resolve the S and P states from the manifold of other ℓ states because of their significant quantum defects. We readily resolve the D state from the manifold of higher ℓ states at zero field by scanning the ir laser frequency because its quantum defect of $\sim 3 \times 10^{-3}$ results in a splitting from the $n = 24$ manifold of ∼1.4 GHz (barely visible on the inset to Fig. 4).

Each of the measurements plotted as a dot in Fig. 4 represents the presence of a peak in the BBR-induced ion signal from the detector (see Sec. III B) shown in Fig. 3 near the interaction region. The ir laser frequency is fixed and the electric field is scanned over a small region in the vicinity of the resonance as indicated by the solid horizontal lines. The dashed lines are the energies calculated by simply diagonalizing the Hamiltonian matrix using the method of Ref. [27]. There is superb overlap between the data points and the energy calculations with no fit or adjustments in this plot. Even the apparent double data points correspond to the energies of different m_ℓ states when the calculation is done in higher order [28].

In these experiments the Rydberg atoms were excited at C and the detector was located at D in Fig. 1. Although it was expected that their lifetime would allow flight for this 10-cm distance, it was not clear what caused their ionization in the detection region. Below we describe very slow but continuous ionization all along the flight path caused by BBR. The spectroscopic measurements and state identification were corroborated by the field ionization measurements described in Sec. III B.

B. Detection of ionized Rydberg atoms

1. Field ionization

We have measured the strength of the ionization signal along the flight path of the atoms. We replaced the upper plate by one having an array of 30 holes of 0.5 mm diam spaced by ∼4 mm arranged in a triangular lattice near its center and mounted the detector just above these holes (C in Fig. 1 and position B in Fig. 3). These changes enabled us to detect the Rydberg atoms by field ionization and to assure that our signals were not compromised by complicated flight paths of the ions resulting from stray fields near the ends of the plates when the detector was at D in Fig. 1 (A in Fig. 3).

The first experiment was to field ionize the Rydberg atoms by applying several hundred volts to the plates. The resulting signals had a field threshold at the correct values given by $\mathcal{E}_{\rm FI} = 5 \times 10^9/16n^4$ V/cm. This direct field ionization corroborated our spectroscopic measurements described in Sec. III A because we could identify the states we chose to excite by $\mathcal{E}_{FI}$ as well as by their optical excitation frequency. Also, the signals were very much larger than those collected previously with the detector at A in Fig. 3 even though the acceptance area was reduced to that of the small holes instead of the partially open, 1.5-cm-aperture of the MCP as shown. Assuming that the applied field ionized all the Rydberg atoms, we conclude that our previous signals were derived from a very small fraction of the total Rydberg population.

When we moved the well-defined location of the sub-mm size laser beams to positions not underneath one of the holes, the field ionization signals vanished because the ions were accelerated directly into the plate. We could map out the position of the holes this way, and the results corroborated their known physical positions.

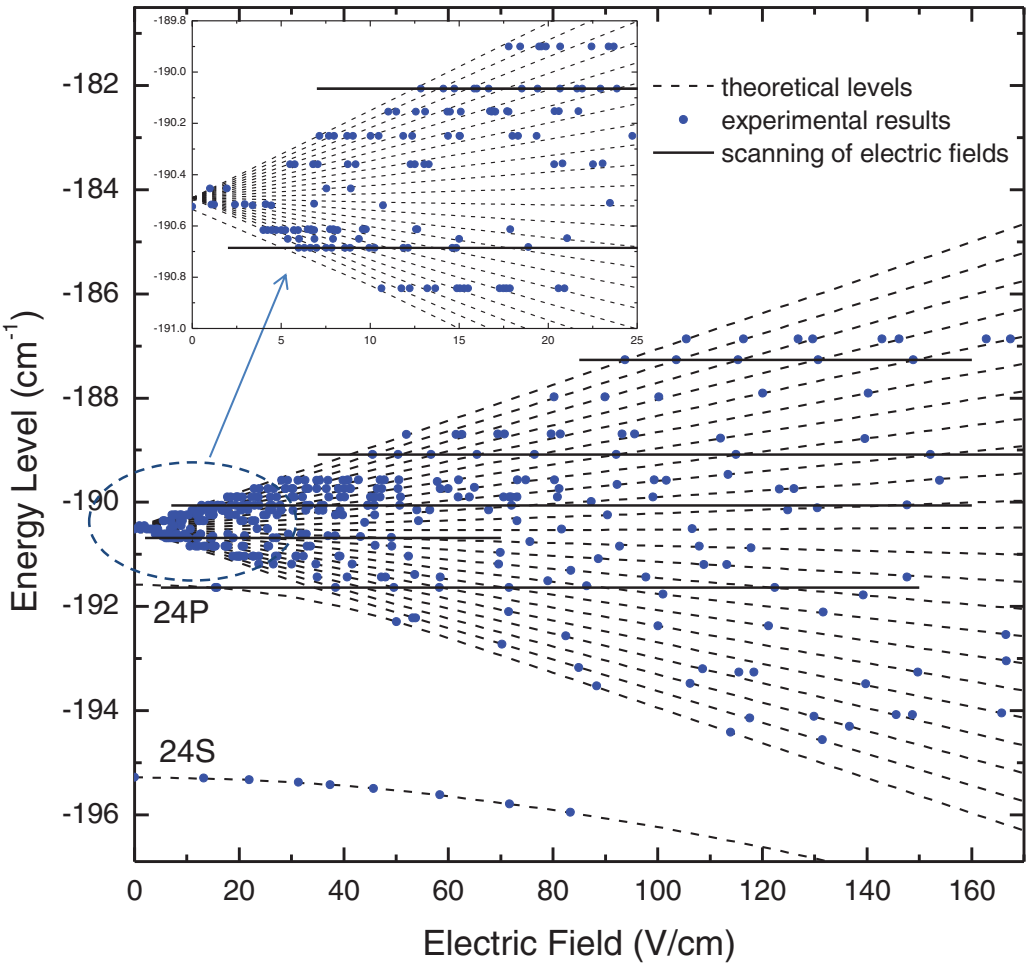

FIG. 4. (Color online) The dashed lines are energy eigenvalues calculated for the $n = 24$ Rydberg states with $m_\ell = 0$ using the method of Ref. [27], and the dots show the location in frequency and field where we observed ion peaks. The solid horizontal lines indicate a few of the field scans with the laser frequency held fixed. The inset is a zoom near the low field region.

2. *Blackbody radiation ionization*

With the applied field set below $\mathcal{E}_{FI}$, there were still ionization signals when the laser frequencies were resonant with transitions to the Rydberg states, but these were very much smaller. Moreover, moving the excitation region defined by the laser beams away from directly under the holes made no noticeable change in the signal strength. This means that the ionization in this case was a slow process, occurring all along the atomic flight paths.

Just beyond the interaction region we used an auxiliary laser beam that drives the $2\ ^3S \rightarrow 2\ ^3P$ transition at $\lambda = 1083$ nm to deflect the metastable $2\ ^3S$ atoms [18,19]. This can be used to measure the remaining fraction of He* atoms after the STIRAP process and thereby determine its absolute efficiency. We moved the Rydberg excitation region upstream considerably and used the average longitudinal velocity of the atoms in the beam to convert the position to time delay. The increase of $2\ ^3S$ population measured with the beam detector slightly displaced transversely from position E in Fig. 1 was used to calculate rates of radiative decay of the $24S$ and $30S$ states. The dominant decay channel from these states is $nS \rightarrow 2\ ^3P \rightarrow 2\ ^3S$ [29] and the last step takes only 0.1 μs. Thus the repopulation time of $2\ ^3S$ is a valid measure of the nS lifetimes. Our measured 11.1(1.1) μs and 19.1(1.6) μs lifetimes agree well with the calculated 9 and 17 μs [29].

An interesting result arose when, with the excitation region moved upstream, we measured the exponential decrease of the ion signal strength. Plots of this signal decrease are shown in Fig. 5 where a single exponential decay has been fitted to the data, and the fit is quite good. Again, we converted the position to time to get the decay lifetimes. We found 16(1) and 34(1) μs for the $24S$ and $30S$ states, respectively, and these lifetimes are significantly longer than the calculated lifetimes. Such slower decays of the ionization signal were completely unexpected, and a possible explanation is in Sec. III B 3.

The measurements described above provide convincing evidence that the signals we detect in the absence of field ionization derive from BBR ionization of a very small fraction of the Rydberg atom population. Our estimated Rydberg excitation rate is $\sim 8 \times 10^7$/s because other measurements suggest that we can excite $\sim 1/3$ of the $\sim 2.5 \times 10^8$ He* emerging from the rectangular aperture at B in Fig. 1 [18,19]. The $24S$ measurements were made $\sim$28 mm downstream from the excitation region, and as Fig. 5 shows, $\sim$75% of the atoms have either decayed or been ionized in this distance, suggesting

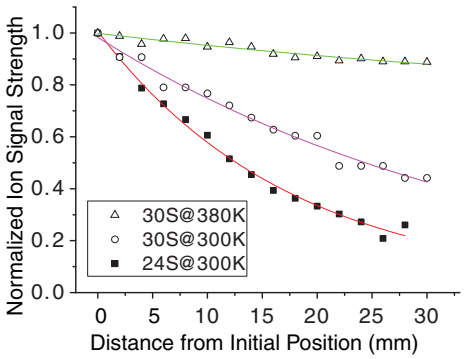

FIG. 5. (Color online) The two lower curves show the decay of the ion signal from the 24*S* and 30*S* states (squares and circles, respectively) taken by moving the laser excitation region upstream from the 25-mm lattice of the holes in the upper plate. For these data the voltage between the plates was just enough to attract the ions through the holes, well below $\mathcal{E}_{FI}$. Since the peak of the atomic beam velocity distribution is at ∼1070 m/s, the 30-mm scale here corresponds to a flight time of ∼28 μs. The uppermost curve (triangles) is for the 30S state with the plates heated to about 380 K.

a flux of $\sim 2 \times 10^7$ Rydberg atoms/s at this point. Our count rate of $\sim 10^5$ was ∼0.5% of this.

We have had direct communication with the authors of Ref. [10] who estimated the rate of direct photoionization of 24*S* Rydberg atoms to be ∼300/s [30]. In the 15 μs that our atoms traveling at 1070 m/s are in the 15-mm field of view of our ion detector, we would expect 0.45% of them to be ionized.

The BBR can also induce transitions from 24*S* to various *P* states, and the strongest such transitions have $\Delta n < 2$ [31]. Thus a few of these can be populated and then ionized by BBR in a two-step process [10], and the combination of ionization by both processes is comparable to our measured ∼0.5 % [30]. Although the rate for each of these two-step processes is small, there are many accessible Rydberg states that provide multiple independent ionization channels so their total contribution is significant. Any three step processes do not contribute significantly.

3. *Rate equation description of reservoir*

There have been several calculations of the ionization and redistribution rates of Rydberg atoms by BBR [8–10] that are in approximate agreement. We have concentrated on Ref. [10] that identifies the two primary BBR ionization channels discussed above. For the two-step processes, the nS states can be driven only to the nP states by electric dipole processes, and their lifetimes are approximately twice those of the *S* states [29].

We have made a rate equation model of the effect of BBR on the particular Rydberg state $|e\rangle$ that we populated. We suppose that $|e\rangle$ can radiatively decay to the $2\ ^3S$ state $|g\rangle$ at rate γ_{eg} and that the BBR can ionize the state $|e\rangle$ directly at rate γ_{ei}, where the subscripts g and i refer to the final state. We also suppose that there is a reservoir of nP states that can be populated by BBR from $|e\rangle$ at a rate γ_{er} [17]. Since these nP states decay more slowly than the nS states where they originated, they can contribute to the ionization signal for a longer time and thereby extend its duration. They can also be further redistributed, but for the purpose of our model we neglect these dynamics and lump all such behavior into γ_{ri} for direct ionization and γ_{rg} for decay to $|g\rangle$. We assume that there are so many states accessible to these reservoir atoms when they are driven by BBR that their rate of return to $|e\rangle$ is negligible. As long as there are some individual reservoir states whose decay rates are slower than $|e\rangle$ and ionize faster than $|e\rangle$, we might expect an ionization signal of longer duration [31].

The rate equations are

$$\dot{N}_e(t) = -\gamma_{eg}N_e - \gamma_{er}N_e - \gamma_{ei}N_e \equiv -\gamma_e N_e \quad (1a)$$

$$\dot{N}_r(t) = \gamma_{er}N_e - \gamma_{rg}N_r - \gamma_{ri}N_r \equiv \gamma_{er}N_e - \gamma_r N_r. \quad (1b)$$

The solution of Eq. (1a) is simply $N_e(t) = N_e(0)e^{-\gamma_e t}$. Then Eq. (1b) is solved by

$$N_r(t) = N_e(0)\gamma_{er}\left[\frac{e^{-\gamma_e t} - e^{-\gamma_r t}}{\gamma_r - \gamma_e}\right]. \quad (2)$$

The current measured by our ion detector is given by $I_i(t) = \gamma_{ei}N_e(t) + \gamma_{ri}N_r(t)$ and we compared this with the repopulation rate of $|g\rangle$ given by $\dot{N}_g(t) = \gamma_{eg}N_e(t) + \gamma_{rg}N_r(t)$. We estimated $\gamma_{eg} \sim 6 \times 10^4$/s from Fig. 2 of Ref. [29] and values of $\gamma_{er} \sim 1.6 \times 10^4$/s, $\gamma_{ei} \sim 400$/s, and $\gamma_{ri} \sim 2 \times 10^3$/s from Fig. 1 of Ref. [10]. Those reservoir states that decay quickly do not contribute much to $I_i(t)$ and for the slower-decaying ones we take $\gamma_{rg} \sim \gamma_{eg}/2$ and $\gamma_{ri} \sim 2\gamma_{ei}$. Plots of $I_i(t)$ and $\dot{N}_g(t)$ then show behavior qualitatively similar to Fig. 5.

This reservoir model was corroborated by two experiments. In the first one, we heated the plates to ∼380 K with a dc current through thermally epoxied resistors mounted on the outside of the plates to increase the BBR intensity, and we observed a strong increase of the ionization signal strength (cooling them is more difficult). The current caused no noticeable electric field effects. The magnitude of these changes is consistent with the results of Ref. [10] and is a most convincing test of the BBR ionization hypothesis. Moreover, in the warm environment, the spatial decay rate (hence temporal rate) was observed to be much slower, as shown by the uppermost data set in Fig. 5. Our rate equation model is also consistent with this further increase in the decay time.

In the second experiment we shined a second beam of the excitation frequency red light onto the atomic beam immediately after the excitation region in the hope of causing stimulated emission back to the $3\ ^3P$ state and subsequent decay to $|g\rangle$ that we could then detect by deflection (see Sec. III B 2). We saw almost none, suggesting that the diffusion from $|e\rangle$ into the reservoir states is significantly faster than γ_{eg}. The fact that the measured $N_g(t)$ shows a time dependence consistent with the calculated lifetimes of Ref. [29] suggests that γ_{rg}, averaged over all the reservoir states, is indeed comparable to γ_{eg}.

C. Study of collisional ionization

We have done several experiments to test for the presence of collisional ionization. To check for the effects of background gas collisions we partially choked off the vacuum pumps so the background pressure rose significantly. There was no appreciable change of the ion signal when normalized to the reduced He* flux. We varied both the He gas flow rate and the

outlet pressure of the source, and similarly saw no significant changes. Finally, we varied the discharge conditions of the source, both current and voltage, with no net observable effect. This series of measurements convinced us that all collisions play a negligible role in ionizing the Rydberg atoms.

D. Testing the laser parameters

In all of these experiments, the excitation process exploited STIRAP to maximize the number of Rydberg atoms [11–13]. That is, the atoms in the beam first encountered the red light in the $\lambda = 785$–815 nm region that connects the $3\,^3P$ state to the nS and nD states and then the $\lambda = 389$ nm for the $2\,^3S \rightarrow 3\,^3P$ transition (see Figs. 2 and 3). To test how well our laser parameters satisfied the STIRAP condition, we exploited the BBR ionization to measure the laser parameters directly.

We optimize our process by measuring both the laser beam profiles and total power and then use this information to compute the spatial dependence of the Rabi frequency of the STIRAP beams from the atomic state transitions matrix elements. Because the 1.5-mm atomic beam height is well inside the 2-mm FWHM vertical laser beam height, the atoms in different parts of the beam experience only a small difference of Rabi frequencies. Since our beam profilometer measurements and the power measurements are accurate to a few %, we are confident of these calculated values of the Rabi frequencies.

Nevertheless, we can check these values using the atoms themselves as probes of the uv laser Rabi frequency by measuring the Autler-Townes splitting of the $3\,^3P$ state. We use the strong uv light to drive the $2\,^3S \rightarrow 3\,^3P$ transition and a reduced power ir beam as a probe of the two-peak separation. Figure 6(a) shows a small sample from our spectra obtained by scanning the ir laser frequency in the region of $\lambda = 792.28$ nm to excite the 30S state in zero applied electric field. The scans in Fig. 6(a) are for various uv powers $P_{\rm uv}$ and Fig. 6(b) shows a plot of the separation between the peaks vs $\sqrt{P_{\rm uv}}$.

The inset to Fig. 6(b) shows the geometry of our setup viewed along the laser beams. The uv beam was expanded to have a FWHM profile of 1.6 mm wide by 1.24 mm high as shown by the larger ellipse, and the red beam was moved to its center and focused to a smaller size of FWHM 0.32 mm wide by 0.66 mm high as shown by the inner ellipse. The horizontal lines show the atomic beam's 1/2-mm width where its profile is flat and maximum, but it has penumbral regions of comparable size above and below. Estimates suggest that 80% of the atoms experience a uv Rabi frequency of at least 85% of the peak value.

We convert $P_{\rm uv}$ to the peak Rabi frequency $\Omega_{\rm uv}$ from our beam profilometer's fitted values of the full width half maximum (FWHM) by first calculating the Gaussian beam waist $w_0 \approx 0.85$ of the FWHM value. We modified the expression for the peak intensity I_c of a circular Gaussian beam for our elliptical case to $I_c = 2P/\pi w_1 w_2$, where P is the total power, and calculate $\Omega_{\rm uv}$ for both the $M_J = \pm 1$ and 0 transitions driven by our linearly polarized light that each have $\Delta M_J = 0$. They are nearly equal so we take a weighted average to find $\Omega_{\rm uv} \approx 2.89\sqrt{P_{\rm uv}}$ with $P_{\rm uv}$ in mW and $\Omega_{\rm uv}$ in MHz. The slope

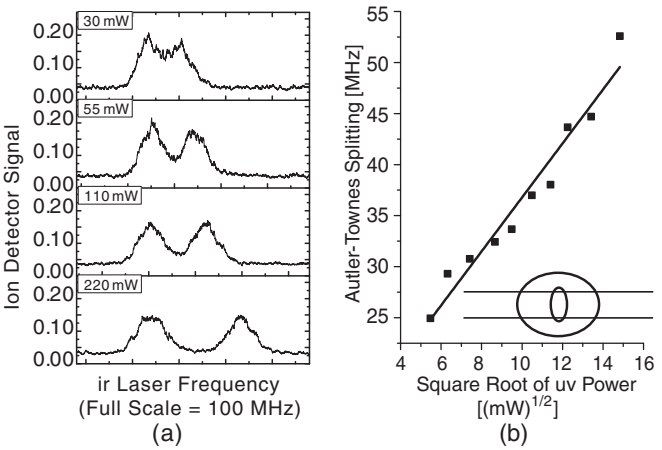

FIG. 6. Part (a) shows a few traces of the measured ionization current derived from Rydberg atoms exposed to both uv and ir light vs. ir frequency. The double peaks are separated by the uv Rabi frequency $\Omega_{\rm uv}$ and constitute the Autler-Townes splitting. Part (b) is a plot of the observed $\Omega_{\rm uv}$ vs. $\sqrt{P_{\rm uv}}$. The inset to part (b) shows the geometry of the two laser beams and the path of the most intense, central part of the atomic beam (see text).

of the fitted straight line in Fig. 6(b) is 2.79(.22) MHz/$\sqrt{P_{\rm uv}}$, and the agreement corroborates our confidence in these measurements, although we think its excellence is somewhat fortuitous.

We have made measurements with the uv light tuned off-resonance and the ir light detuned accordingly and observed the expected asymmetrical peak heights as the ir laser frequency is scanned. This provides additional confidence of our knowing the nature of the light field that the atoms experience. The individual peaks of Fig. 6(a) have a FWHM of ~12 MHz that may arise from a variety of effects such as power broadening from the ir probe light (~4 MHz), residual variation of uv laser intensity in the smaller ir probe region (~4 MHz), laser frequency jitter (~1 or 2 MHz), residual stray electric fields (~1 MHz), and so on.

IV. SUMMARY AND CONCLUSIONS

We have measured the Stark spectra of Rydberg states of He with large S/N using only the ambient BBR to produce the ionized Rydberg atoms we detect. Support for ion production by BBR comes from several conclusive experiments and no additional fields are required. The two step Rydberg excitation route is performed in the STIRAP configuration with the eventual goal of an absolute STIRAP efficiency measurement.

We have measured the time dependence of the decay of the ionization signal as well as of the repopulation of the ground state and found quite different rates. We attribute this difference to the population of multiple states in a reservoir of the Rydberg levels, some of which radiatively decay to $2\,^3S$ more slowly and ionize faster than the laser-populated state $|e\rangle$. We have modeled the process with rate equations that show similar behavior to our measurements. We have exploited the BBR ionization to use the Autler-Townes splitting as a laser-beam diagnostic.

ACKNOWLEDGMENTS

We wish to acknowledge very helpful contributions in the earlier stages of this work by Oleg Kritsun, S.-H. Lee, Andreas Vernaleken, and Jonathan Kaufman (deceased). We also acknowledge invaluable Stark map calculations by Tom Bergeman and careful reading of the manuscript by M. G. Cohen. This work was supported by ONR.

[1] Thomas Gallagher, *Rydberg Atoms* (Cambridge University Press, Cambridge, UK, 1994).
[2] T. F. Gallagher and W. E. Cooke, Phys. Rev. Lett. **42**, 835 (1979).
[3] W. E. Cooke and T. F. Gallagher, Phys. Rev. A **21**, 588 (1980).
[4] John W. Farley and William H. Wing, Phys. Rev. A **23**, 2397 (1981).
[5] William P. Spencer, A. Ganesh Vaidyanathan, Daniel Kleppner, and Theodore W. Ducas, Phys. Rev. A **24**, 2513 (1981).
[6] William P. Spencer, A. Ganesh Vaidyanathan, Daniel Kleppner, and Theodore W. Ducas, Phys. Rev. A **25**, 380 (1982).
[7] William P. Spencer, A. Ganesh Vaidyanathan, Daniel Kleppner, and Theodore W. Ducas, Phys. Rev. A **26**, 1490 (1982).
[8] I. I. Ryabtsev, D. B. Tretyakov, I. I. Beterov, N. N. Bezuglov, K. Miculis, and A. Ekers, J. Phys. B **38**, S17 (2005) (Special Issue on Rydberg Physics).
[9] I. I. Beterov, D. B. Tretyakov, I. I. Ryabtsev, A. Ekers, and N. N. Bezuglov, Phys. Rev. A **75**, 052720 (2007).
[10] I. L. Glukhov, E. A. Nekipelov, and V. D. OvsiannikovJ. Phys. B **43**, 125002 (2010).
[11] U. Gaubatz, P. Rudecki, M. Becker, S. Schiemann, M. Kulz, and K. Bergmann, Chem. Phys. Lett. **149**, 463 (1988).
[12] U. Gaubatz, P. Rudecki, S. Schiemann, and K. Bergmann, J. Chem. Phys. **92**, 5363 (1990).
[13] K. Bergmann, H. Theuer, and B. W. Shore, Rev. Mod. Phys. **70**, 1003 (1998).
[14] W. Süptitz, B. C. Duncan, and P. L. Gould, JOUOSAB **14**, 1001 (1997).
[15] B. C. Duncan, V. Sanchez-Villicana, P. L. Gould, and H. R. Sadeghpour, Phys. Rev. A **63**, 043411 (2001).
[16] T. Cubel, B. K. Teo, V. S. Malinovsky, J. R. Guest, A. Reinhard, B. Knuffman, P. R. Berman, and G. Raithel, Phys. Rev. A **72**, 023405 (2005).
[17] Wenhui Li *et al.*, Phys. Rev. A **70**, 042713 (2004).
[18] Xiaoxu Lu, Ph.D. thesis, Stony Brook University, 2011.
[19] Xiaoxu Lu, Yuan Sun, and Harold Metcalf (in preparation).
[20] O. Kritsun, O. Boiko, and H. Metcalf, Bull. Am. Phys. Soc. **49**, 24 (2004), D1 26.
[21] S.-H. Lee, A. Vernaleken, K. Choi, J. Kaufman O. Kritsun, and H. Metcalf, "Efficient Rydberg Excitation of He with STIRAP" in Frontiers in Optics, OSA Technical Digest (CD) (Optical Society of America, Rochester, NY, 2006), paper JWD122.
[22] X. Lu, Y. Sun, C. Allred, and H. Metcalf, Bull. Am. Phys. Soc. **55**, 115 (2010), M1 153.
[23] J. Kawanaka, M. Hagiuda, K. Shimizu, F. Shimizu, and H. Takuma, Appl. Phys. B. **56**, 21 (1993).
[24] H. C. Mastwijk, M. van Rijnbach, J. W. Thomsen, and P. van der Straten, and A. Niehaus, Eur. Phys. J. D **4**, 131 (1998).
[25] The frequency stabilization for this uv light actually has both a fast and slow loop. The fast loop uses the Pound-Drever-Hall scheme [26] to lock the TiS at $\lambda = 778$ nm to a Fabry-Perot cavity with high mechanical and thermal stability. The slow, long-term stabilization uses saturation spectroscopy that locks the $\lambda = 389$ nm light to the He* transition. The signal is derived from a sealed cell of He with a weak rf discharge that populates the $2\ ^3S_1$ state. The addition of this extra locking loop showed negligible effect on the short-term linewidth of the TiS. The entire system provides 400 mW of uv power with frequency stability $\sim$250 kHz (full rms in a 300-Hz bandwidth) and is modulated by 400 kHz at a rate of 2 kHz for the lock.
[26] R. W. Drever and J. L. Hall, App. Phys. B **31**, 97 (1983).
[27] Michael G. Littman, Myron L. Zimmerman, Theodore W. Ducas, Richard R. Freeman, and Daniel Kleppner, Phys. Rev. Lett. **36**, 788 (1976).
[28] H. A. Bethe and E. E. Salpeter, *Quantum Mechanics of One- and Two-Electron Atoms* (Springer-Verlag, Berlin, 1957) [Also published by Dover, New York, 2008 (paperback)].
[29] Constantine E. Theodosiou, Phys. Rev. A **30**, 2910 (1984).
[30] Igor Glukhov (private communication).
[31] E. J. Galvez, J. R. Lewis, B. Chaudhuri, J. J. Rasweiler, H. Latvakoski, F. De Zela, E. Massoni, and H. Castillo, Phys. Rev. A **51**, 4010 (1995).